Robust magnetic field-free switching of a perpendicularly magnetized free layer for SOT-MRAM

R.L. de Orio[a,*], A. Makarov[b], S. Selberherr[b], W. Goes[c], J. Ender[a], S. Fiorentini[a], V. Sverdlov[a]

[a] Christian Doppler Laboratory for Nonvolatile Magnetoresistive Memory and Logic at the Institute for Microelectronics, TU Wien, Vienna, Austria
[b] Institute for Microelectronics, TU Wien, Gußhausstraße 27-29/E360, 1040 Vienna, Austria
[c] Silvaco Europe Ltd., Cambridge, United Kingdom

ARTICLE INFO

ABSTRACT

We investigate the robustness of a purely electrical field-free switching of a perpendicularly magnetized free layer based on SOT. The effective magnetic field which leads to deterministic switching of a rectangular as well as of a square free layer is created dynamically by a two-current pulse scheme. It is demonstrated that the switching is very robust, being insensitive to fluctuations of the write pulses' durations and to relatively large variations of the heavy metal wires' dimensions. Furthermore, it remains reliable for a wide range of synchronization failures between the pulses. The combination of a rectangular free layer shape with a partial overlap with the second current line accelerates the switching of the cell allowing a fast, 0.25 ns, switching.

1. Introduction

The development of memories has been supported by the continuous downscaling of the semiconductor devices. This scaling has been followed, however, by an increasing standby power consumption due to the volatile nature of the classical static random access memory (SRAM) and dynamic random access memory (DRAM), an issue which can be improved with the use of nonvolatile memories. Nevertheless, this is only possible if the operation characteristics of the nonvolatile memories are comparable to those of SRAM or DRAM.

Besides the charge, the spin is also an inherent property of the electron, which can be exploited. Magnetic tunnel junctions (MTJ), formed by two ferromagnetic layers separated by a tunnel barrier, are the key elements of magnetoresistive random access memory (MRAM) [1–3]. Their parallel and anti-parallel arrangement of the magnetization in the ferromagnetic layers and the corresponding low and high resistance states make this spin-based technology a feasible energy-efficient and non-volatile alternative to charge-based memories.

Spin-transfer torque MRAM (STT-MRAM) is fast, possesses high endurance, and has a simple structure. It is compatible with CMOS technology and can be straightforwardly embedded in circuits [4]. It is also promising for use in system on chip (SoC) circuits as a replacement of conventional flash memory, as well as for embedded applications [5].

Although the use of STT-MRAM in last-level caches is possible [6], the switching current for operating with pulses faster than 10 ns is fairly high [7]. The large current densities flowing through the MTJs lead to oxide reliability issues which in turn reduce the MRAM endurance.

Spin-orbit torque (SOT) assisted switching of a magnetic free layer (FL) is promising, because it combines non-volatility, high-speed, and high-endurance [8]. In this memory the read and write current paths are separated in such a way that the relatively high write current does not pass through the MTJ, while only a much smaller read current is applied through the MTJ. Since the large write current does not flow through the MTJ, the tunnel barrier is prevented from damage and the device reliability is improved. However, a static magnetic field is still required for deterministic switching [9] of the FL. Even though several alternatives to build in the field source in the cell [10,11] or to break the cell mirror symmetry to achieve a field-free switching were reported, cf. [12–20] these require a local intrusion into the cell fabrication, which complicates the large scale integration. Recently, an interesting field-free scheme has been demonstrated based on stacking of a ferromagnetic layer and heavy metals with opposite spin Hall angles [21].

A purely electrical magnetic field-free switching of a perpendicular FL by two consecutive orthogonal current pulses was first reported in [22,23]. In this work we extend the study by focusing on the reliability of the switching. It is demonstrated that the switching is very robust, being insensitive to fluctuations of the write pulses' durations and to relatively large variations of the heavy metal wires' dimensions. In

---

* Corresponding author.
  E-mail address: orio@iue.tuwien.ac.at (R.L. de Orio).
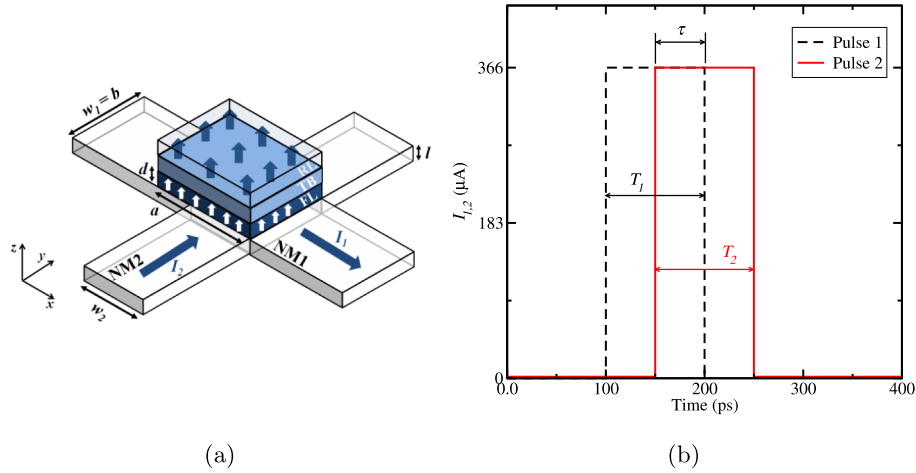
Fig. 1. (a) Schematic SOT cell with a perpendicularly magnetized FL. The switching is realized through the application of current pulses to the NM1 and NM2 wires. Square and rectangular FLs are considered by choosing appropriate values for a and b. The overlap of the NM2 wire with the FL is determined by w_2. (b) Example of current pulses applied to NM1 and NM2.

addition, the switching scheme is reliable for a wide range of synchronization failures between the pulses.

2. Free layer switching based on SOT

In the SOT-MRAM cell the MTJ FL is grown on a heavy normal metal (NM) wire with a large spin Hall angle [24]. Fig. 1(a) depicts a SOT-MRAM cell formed with a perpendicularly magnetized FL studied here. The FL dimensions are $a \times b \times d = 25 \times 10 \times 2$ nm^3, where a represents the length, b represents the width, and d is the thickness of the FL. The heavy metal wires, NM1 and NM2, both have a thickness of $l = 3$ nm.

The electric current which passes through the NM1 wire generates a transverse flow of spin-polarized electrons in the z direction due to the spin Hall effect. This spin current generates a torque on the magnetization of the FL. This torque aids to put the magnetization in the plane of the FL perpendicular to the current, if the applied current is sufficiently high to exceed the critical current density

$$J_C = \frac{2e}{\hbar} \frac{M_S d}{\theta_{SH}} \left(\frac{H_K^{eff}}{2} - \frac{H_{ext}}{\sqrt{2}} \right),$$
(1)

where e is the elementary charge, $\hbar$ is the Plank constant, M_S is the saturation magnetization, d is the thickness of the FL, θ_{SH} is the effective spin Hall angle, and H_K^{eff} is the effective anisotropy field. In order to drive the magnetization towards the $-z$ direction, thus completing the switching deterministically, an external magnetic field, H_{ext}, has to be applied.

In order to accomplish the FL magnetization switching without an external magnetic field a two-current pulse scheme is used [22,23]. Here, a second heavy metal wire (NM2) is placed perpendicularly to the first heavy metal wire (NM1) as shown in Fig. 1(a). Depending on the values of the lateral dimensions, a and b, a square or a rectangular FL is considered.

The switching of the FL magnetization is initiated with the application of a first current pulse through the NM1 wire. This pulse brings the magnetization in the plane of the FL as discussed. Instead of an external field, a second current pulse through the NM2 wire is applied to drive the magnetization reversal. An example of a current pulse configuration is depicted in Fig. 1(b). The reading operation of the cell is carried out by applying a current through the MTJ which is grown on the FL and measuring its corresponding tunneling magnetoresistance ratio (TMR).

3. Modeling

The magnetization switching dynamics of the FL is described by the Landau-Lifshitz-Gilbert equation with the torques [25,26]

$$\frac{\partial \mathbf{m}}{\partial t} = -\mu_0 |\gamma| \mathbf{m} \times \mathbf{H}_\Sigma + \alpha \mathbf{m} \times \frac{\partial \mathbf{m}}{\partial t} + \frac{1}{M_S} \mathbf{T_S},$$
(2)

where $\mathbf{m}$ is the position-dependent magnetization, $\mathbf{M}$, normalized by the saturation magnetization, M_S, γ is the gyromagnetic ratio, μ_0 is the vacuum magnetic permeability, $\mathbf{H}_\Sigma$ is the magnetic field defined below, and α is the Gilbert damping. The first term on the right-hand side describes a precession of the magnetization around the field $\mathbf{H}_\Sigma$, the second term describes a damping mechanism, which tries to align the magnetization with the field $\mathbf{H}_\Sigma$, and the third term corresponds to the generated SOT, $\mathbf{T_S}$.

The magnetic field, $\mathbf{H}_\Sigma$, is a combination of several contributions, namely, the exchange field ($\mathbf{H_{ex}}$), the uniaxial perpendicular anisotropy field ($\mathbf{H_K}$), the demagnetizing field ($\mathbf{H_{demag}}$), the external field ($\mathbf{H_{ext}}$), the magnetic field generated by the current pulses ($\mathbf{H_{amp}}$), and the random thermal field ($\mathbf{H_{thermal}}$), thus given by

$$\mathbf{H}_\Sigma = \mathbf{H_{ex}} + \mathbf{H_K} + \mathbf{H_{demag}} + \mathbf{H_{ext}} + \mathbf{H_{amp}} + \mathbf{H_{thermal}},$$
(3)

with

$$\mathbf{H_{ex}} = \frac{2A}{\mu_0 M_S} \nabla^2 \mathbf{m},$$
(4)

$$\mathbf{H_K} = \frac{2K}{\mu_0 M_S} (\mathbf{m} \cdot \mathbf{n}) \mathbf{n},$$
(5)

where A is the exchange constant, K is the perpendicular anisotropy constant, and $\mathbf{n}$ is the easy-axis direction of the anisotropy, which is assumed out-of-plane.

The SOT term, $\mathbf{T_S}$ in (2), are taken in the form [27]

$$\mathbf{T_S} = -c_j \mathbf{m} \times (\mathbf{m} \times \hat{s}) + \beta c_j (\mathbf{m} \times \hat{s}).$$
(6)

Here, $\hat{s} = \hat{j} \times \hat{z}$ gives the spin polarization direction, with $\hat{j}$ being the current density unit vector, and β is a measure of the field-like torque, which is neglected for the most part of this work. This assumption will be justified later. The SOT is proportional to the applied current density, j, through the parameter c_j, given by

$$c_j = \gamma \frac{\hbar}{2e} \frac{\theta_{SH}}{d} j.$$
(7)

The set of Eqs. (2)–(7) can be solved numerically to describe the

Table 1

Parameters used in the simulations. This set of parameters corresponds to heavy metal wires made of tungsten, while the magnetic FL is of CoFeB on MgO [27].

Saturation magnetization, M_S	1×10^6 A/m
Exchange constant, A	1×10^{-11} J/m
Effective perpendicular anisotropy, K	9.0×10^5 J/m^3
Gilbert damping, α	0.02
Spin Hall angle, θ_{SH}	0.3
Demagnetizing coefficient, D	0.69

switching dynamics of a SOT cell. The parameters are from [27] and given in Table 1.

The thermal stability factor is given by [4,28]

$$\Delta = \left(K - D \frac{\mu_0 M_S^2}{2} \right) \frac{V}{k_B T}, \tag{8}$$

where K is the average uniaxial anisotropy energy density which can involve bulk and interfacial anisotropies, D is the demagnetizing coefficient, V is the volume of the FL, k_B is the Boltzmann constant, and T is the temperature. $D \approx D_z - D_x$, where D_z and D_x are the demagnetizing factors for rectangular cuboids, which are determined based on [29].

For standalone memory a thermal stability factor of about 80 is normally required [4]. However, this requirement can be relaxed for typical SRAM applications, like cache memories, in view of a faster operation. In this case, a smaller thermal stability factor is acceptable [30]. For the structures studied in this work a thermal stability factor of about 55 is estimated.

As Fig. 1(a) shows, the FL fully overlaps with the NM1 wire. Thus, the width of the NM1 wire is $w_1 = 10$ nm. On the other hand, NM2 wires of different widths, 10 nm $\leqslant w_2 \leqslant$ 25 nm, have been considered. This determines the overlap of the FL with the NM2 wire. As it will be shown, a proper overlap improves the switching speed and, furthermore, leads to a very robust switching with the help of the second current pulse.

The two current pulses of the field-free scheme described in Section 2 are applied to the NM1 and NM2 wires (Fig. 1). The first pulse, applied to the NM1 wire, has a fixed duration of $T_1 = 100$ ps and a fixed current I_1. Since the critical current density for switching is about 10^{13} A/m^2, the current is set to provide a current density of $j_1 = 12 \times 10^{12}$ A/m^2. Then, a second, consecutive and perpendicular pulse is applied through the NM2 wire. This pulse is configured to provide the same current density as the first one. However, the second

current pulse has a variable duration, T_2, in order to investigate the effect of different pulse configurations on the switching dynamics.

An additional parameter considered in this study is the delay/overlap, τ, between the two pulses. A positive value of this parameter indicates a delay between the first and the second pulse, while a negative value indicates an overlap. In this way, the robustness of the scheme in relation to pulse synchronization failures is evaluated. For instance, Fig. 1(b) shows the configuration for pulses with $I_1 = I_2 = 366 \mu$A, $T_1 = T_2 = 100$ ps, and $\tau = -50$ ps.

The combination of (2), (6), and (7) yields ($\beta = 0$)

$$\frac{\partial \mathbf{m}}{\partial t} = -\mu_0 |\gamma| \mathbf{m} \times \mathbf{H}_\Sigma + \alpha \mathbf{m} \times \frac{\partial \mathbf{m}}{\partial t} - \gamma \frac{\hbar}{2e} \frac{\theta_{SH}}{M_S d} [\mathbf{m} \times (\mathbf{m} \times (\mathbf{j_1} \times \mathbf{z}))] \Theta$$

$$(t, T_1) - \gamma \frac{\hbar}{2e} \frac{\theta_{SH}}{M_S d} [\mathbf{m} \times (\mathbf{m} \times (\mathbf{j_2} \times \mathbf{z}))] \Theta(t, T_1, T_2, \tau), \tag{9}$$

for the magnetization dynamics of the two-pulse scheme, where $\Theta(\cdot)$ is the step function which determines when the pulses are active. The solution of (9) yields the components of the magnetization vector $\mathbf{m}$ as a function of time. The field $\mathbf{H}_\Sigma$ includes all terms given in (3), however with $\mathbf{H_{ext}} = 0$. A random thermal field at 300 K is considered. (9) is solved using an in-house open-source tool [31,32] based on the finite difference discretization method.

4. Results

We consider, initially, a cell with a rectangular FL with full overlap with the NM2 wire, sketched in Fig. 2(b). Fig. 2(a) shows the z-component of the magnetization vector as a function of time for different durations of the second pulse, T_2. The magnetization is taken as the average of 20 different realizations (due to the random thermal field) for the same current pulse configuration. Deterministic switching of the FL occurs, i.e. all realizations lead to switching, provided that the pulse duration is not too short.

Fig. 3 shows the magnetization vector distribution in the FL after the first and the second current pulse are applied. After the first current pulse is turned on, the magnetization is put in the plane of the FL (first SOT term in (9)) along the y direction, as shown in Fig. 3(a). Then, the second pulse is turned on ($\tau = 0$), which tilts the magnetization of the whole FL towards the -x direction (second SOT term in (9)), as shown in Fig. 3(b). Since the FL and the wires are fully overlapping, the magnetization of the whole FL is affected resulting in a nearly uniform magnetization distribution. The magnetization experiences the shape anisotropy field which plays the role of an external field and makes the

(a)   (b)
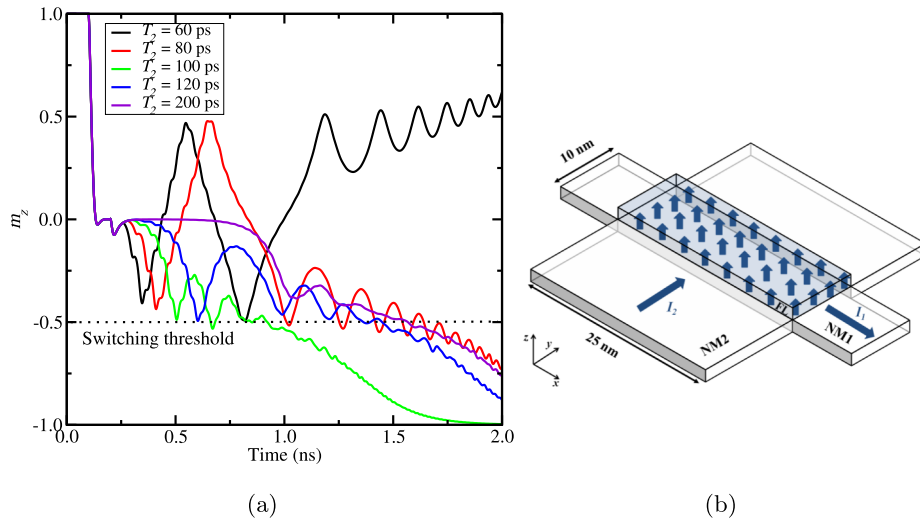
Fig. 2. (a) Average z-component of the magnetization from 20 realizations (due to the random thermal field) as a function of time with T_2 as parameter for (b) the rectangular FL with $w_2 = 25$ nm. The simulations consider $T_1 = 100$ ps and $\tau = 0$. The dotted line indicates the threshold to determine the switching time.
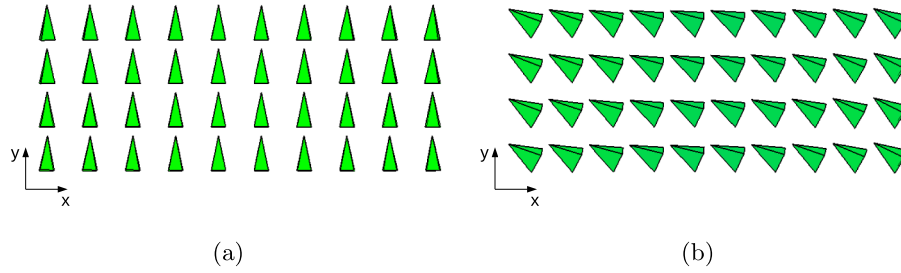
Fig. 3. Snapshot of the magnetization vector (a) after the first pulse and (b) after the second pulse is applied for the rectangular FL with $w_2 = 25$ nm, $T_1 = T_2 = 100$ ps, and $\tau = 0$. The vector colors correspond to the RGB content defined by m_z, where red, green, and blue correspond to $m_z = +1$, $m_z = 0$, and $m_z = -1$, respectively. (For interpretation of the references to colour in this figure legend, the reader is referred to the web version of this article.)
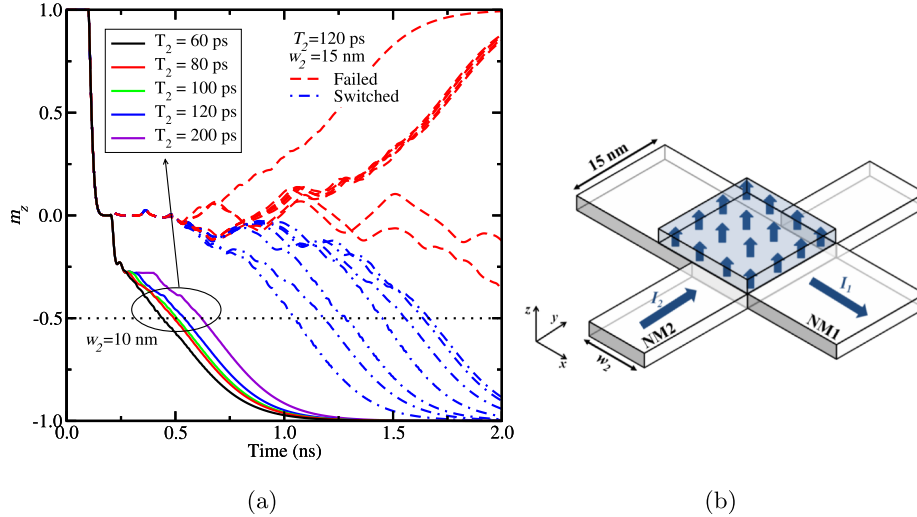

Fig. 4. (a) m_z as a function of time for (b) the square FL. Solid lines: Average m_z simulation for $w_2 = 10$ nm with T_2 as parameter. Dashed lines: several realizations of m_z due to the random thermal field for $w_2 = 15$ nm and $T_2 = 120$ ps. All simulations are carried out with $T_1 = 100$ ps and $\tau = 0$.

switching deterministic.

Considering now a cell with a square FL with $a \times b \times d = 15 \times 15 \times 2$ nm³, $w_2 = 15$ nm, Fig. 4(b), a typical plot of the magnetization component m_z for several realizations is shown by the dashed lines in Fig. 4(a). One can see that the switching is non-deterministic, i.e. part of the realizations switch, part of the realizations do not. In contrast to the cell with the rectangular FL, the magnetization does not experience the shape anisotropy field in the square FL. Therefore, there is no field to support the magnetization reversal and the switching/non-switching distribution is a consequence of the random thermal field. Thus, the switching becomes unreliable.

Reducing the width of the NM2 wire, so that the square FL is only partially overlapping with the NM2 wire [33], the resulting magnetization dynamics for $w_2 = 10$ nm is shown by the solid lines in Fig. 4(a). Reliable switching is observed for all values of T_2. Moreover, the switching time lies in the range of 0.5 ns–0.7 ns, significantly reduced in comparison to the results shown in Fig. 2(a) for the cell with the rectangular FL with full overlap. For instance, for $T_2 = 100$ ps, the switching time of this cell is 0.9 ns, while for the cell with the square FL with a partial NM2 wire overlap it is 0.5 ns. The switching time is taken from the average magnetization curve at the time when $m_z = -0.5$.

Fig. 5 shows the position-dependent magnetization just after the write pulses are applied for the square FL. Similarly to Fig. 3, after the first pulse the magnetization lies in the plane of the FL. Then, due to the SOT of the second pulse, since the NM2 wire is in contact with only part of the FL, just the magnetization under the NM2 wire rotates towards the -x direction, which is shown in Fig. 5(b). The magnetization under the NM2 wire creates a dipolar field which acts as an in-plane magnetic field for the rest of the FL. This field makes the magnetization of the rest
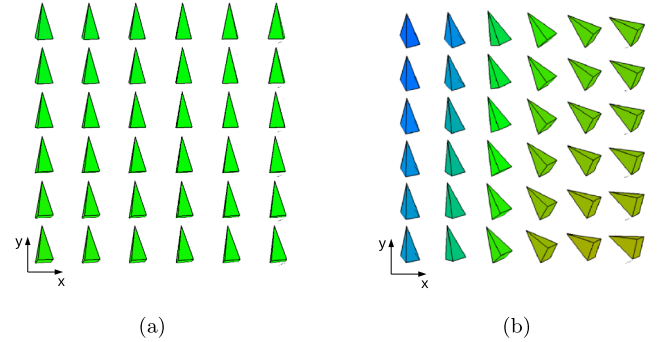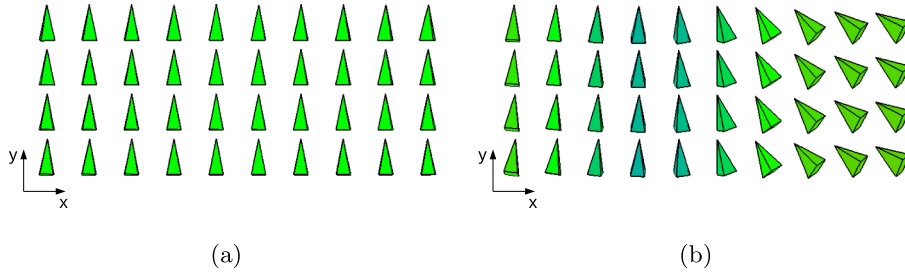

Fig. 5. Snapshot of magnetization (a) after the first pulse and (b) after the second pulse is applied. The simulation parameters are $w_2 = 10$ nm, $T_1 = T_2 = 100$ ps, and $\tau = 0$.

of the FL to precess away from its in-plane orientation, which leads to a reliable switching of the cell with the square FL [33]. The whole magnetization of the FL precesses in the same manner, which is the reason for the robustness with respect to T_2 variations.

Given the beneficial outcome of reducing the width of the NM2 wire for the cell with the square FL, we now reduce the width of the NM2 wire for the cell with the rectangular FL, thus reducing the overlap between the FL and the NM2 wire (Fig. 1(a)). The switching times for this cell are shown in Fig. 6(a), together with the switching times for the cells with the square FL ($w_2 = 10$ nm) and the rectangular FL with full overlap ($w_2 = 25$ nm). In this case, the magnetization in the FL part subject to SOT of the second current is quickly rotated in-plane along
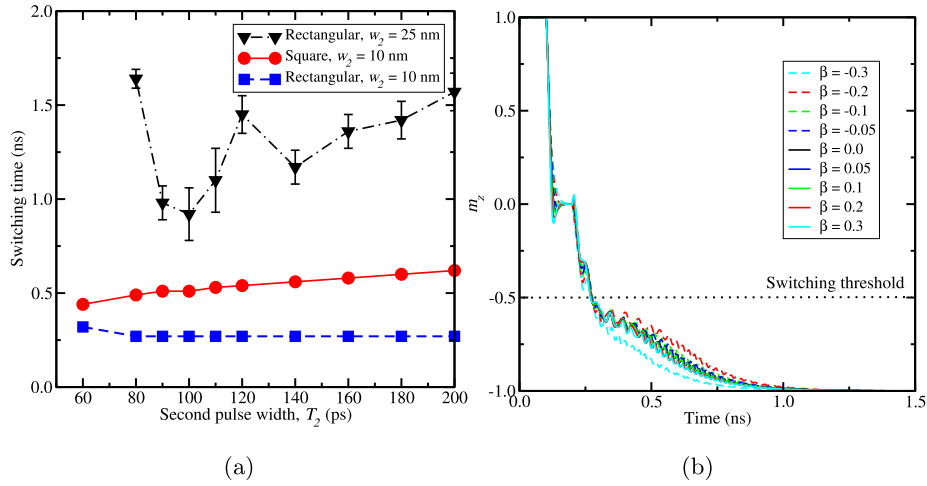
Fig. 6. (a) Switching time as function of T_2 for the cell with the rectangular FL with full and partial overlap with the NM2 wire. The symbols represent the average of 20 realizations. For the structures with $w_2 = 10$ nm the variation of the switching times is smaller than the size of the symbol. (b) Magnetization switching for several values of the field-like parameter β. The simulations are carried out for the cell with the rectangular FL with $w_2 = 10$ nm, current pulses with $T_1 = T_2 = 100$ ps, and $\tau = 0$.

Fig. 7. Snapshot of the magnetization vector (a) after the first pulse and (b) after the second pulse is applied for the rectangular FL with $w_2 = 10$ nm, $T_1 = T_2 = 100$ ps, and $\tau = 0$.

the long edges of the rectangle (Fig. 7(b)). The resulting dipolar field makes the rest of the FL magnetization to precess around it, moving the magnetization deterministically from its in-plane orientation. The switching time is not only shorter, but also its variation as a function of the second pulse duration is reduced.

Note that for the cell with the rectangular FL with smaller overlap a switching time of about 0.25 ns remains practically the same for all pulse durations. It should be noted that this result is accomplished using a smaller current for the second pulse, since the reduction of w_2 implies a decrease of the current magnitude, provided that the current density remains constant.

The SOT given in (6) includes the field-like torque term. This term is taken into account through the parameter β, which has been neglected so far. Fig. 6(b) shows the magnetization component m_z as a function of time for several values of β. The simulations are carried out for the cell with the rectangular FL with $w_2 = 10$ nm. The traces of the magnetization are very similar and the switching times remain practically the same for all cases. This shows that the field-like torque term does not influence the switching and our assumption of $\beta = 0$ is justified. Alternatively, the negligible impact of this term is another evidence of the robustness of the scheme.

In order to verify the impact of variations of the NM2 wire width on the switching time, the NM2 wire width is varied in the range $10 \leqslant w_2 \leqslant 25$ nm for cells with a rectangular FL. Fig. 8 shows the switching times as a function of the NM2 wire width, w_2, and also of the second pulse duration, T_2. The minimum switching times, about 0.25 ns, are obtained for $10 \leqslant w_2 \leqslant 15$ nm, remaining constant for all range of T_2. Increasing w_2 leads to a longer switching time and, as it approaches the full overlap condition, the switching becomes more sensitive to T_2.

So far, the above results have considered a perfect synchronization
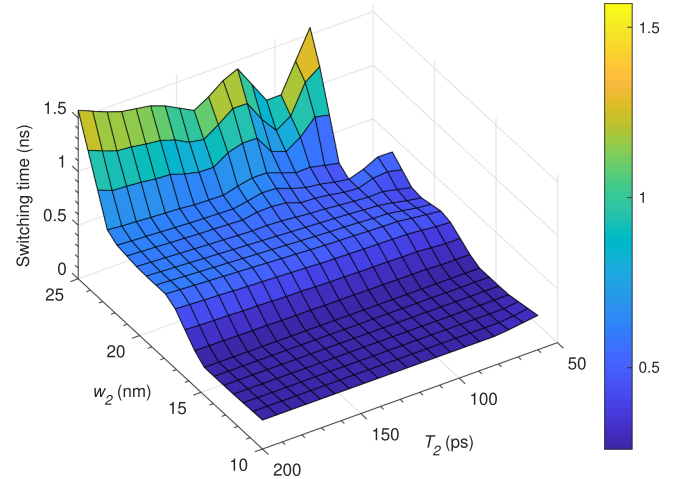
Fig. 8. Switching time as function of the the second wire width and the second pulse duration. The simulations are carried out considering $\tau = 0$.

between the two pulses, i.e. $\tau = 0$ in Fig. 1(b). In practice, however, it is expected that this ideal condition is not given and a delay or an overlap between the pulses can occur as the signals propagate through the interconnect wires. Thus, the impact of these synchronization failures on the switching performance has been investigated. The analysis covers a large range of delay/overlap values, from a 100% overlap between the two pulses ($\tau = -100$ ps) to 100% time delay ($\tau = +100$ ps) in relation to the pulses' width.

The results are shown in Fig. 9 together with the dependence on w_2.
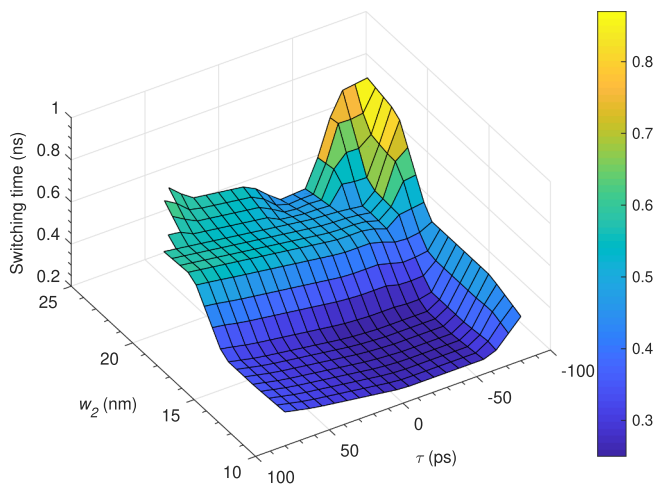
Fig. 9. Switching time as function of the delay/overlap of the pulses and the second wire width. A positive value of τ indicates a delay between the first and the second pulse, while a negative value indicates an overlap. The current pulses assume $T_1 = T_2 = 100$ ps.

A larger overlap or delay between the pulses becomes an issue mainly as w_2 is increased. For a large w_2 in combination with a long delay between the first and the second pulse the switching becomes non-deterministic. However, for smaller values of w_2 the switching times remain very close to the minimum value in the range $-50 \leqslant \tau \leqslant +50$ ps, i.e. up to a 50% of overlap or delay between the first and the second pulse. It is interesting to note that even for a delay as large as 50% the switching time is close to that of the perfectly synchronized pulses and the switching is still fast and reliable. This demonstrates that the switching scheme is also very robust against synchronization failures.

The simulations assume that there is no current leak between the NM1 and NM2 wires, when the two current pulses are on at the same time. This requires that the NM wires have similar resistances, which has to be considered during the design process. Also, the simulations assume perfect rectangular pulses which cannot be obtained in a practical implementation of a memory circuit. Nevertheless, as the switching is reliable for a wide range of pulses durations and synchronization window, the impact of non-ideal pulse shapes is not expected to be an issue for the switching scheme.

5. Conclusion

A very robust and fast field-free switching of a perpendicularly magnetized FL based on SOT is demonstrated. The effective magnetic field which leads to deterministic switching of cells with a rectangular as well as with a square FL is created dynamically by a two-current pulse scheme. When the second current SOT is applied only to a partial region of the FL, namely the region which is in contact with the second heavy metal, the switching speed is increased. The switching times also become practically insensitive to variations of the pulse durations and to possible delays or overlaps between the current pulses. This can be achieved for a relatively large range of the second current line width, which is very beneficial, since the scheme does not require a precise patterning of the second current line.

References

[1] Wolf SA, Awschalom DD, Buhrman RA, Daughton JM, von Molnár S, Roukes ML, Chtchelkanova AY, Treger DM. Spintronics: a spin-based electronics vision for the future. Science 2001;294:1488–95. https://doi.org/10.1126/science.1065389.

[2] Tehrani S, Slaughter JM, Chen E, Durlam M, Shi J, DeHerren M. Progress and outlook for MRAM technology. IEEE Trans Magn 1999;35:2814–9. https://doi.org/10.1109/20.800991.

[3] Tehrani S, Slaughter JM, Deherrera M, Engel BN, Rizzo ND, Salter J, Durlam M, Dave RW, Janesky J, Butcher B, et al. Magnetoresistive random access memory using magnetic tunnel junctions. Proc IEEE 2003;91:703–14. https://doi.org/10.1109/JPROC.2003.811804.

[4] Apalkov D, Dieny B, Slaughter JM. Magnetoresistive random access memory. Proc IEEE 2016;104:1796–830. https://doi.org/10.1109/JPROC.2016.2590142.

[5] Golonzka O, Alzate J-G, Arslan U, Bohr M, Bai P, Brockman J, et al. MRAM as Embedded Non-Volatile Memory Solution for 22FFL FinFET. Technology, Proc. of the 2018 IEDM 2018;18(1). https://doi.org/10.1109/IEDM.2018.8614620. pp. 1–18.1.4.

[6] Jan G, Thomas L, Le S, Lee Y-J, Liu H, Zhu J, et al. Achieving Sub-ns Switching of STT-MRAM for Future Embedded LLC Applications through Improvement of Nucleation and Propagation Switching Mechanisms. Proc. of the 2016 IEEE Symposium on VLSI Technology 2016. p. 1–2. https://doi.org/10.1109/VLSIT.2016.7573362.

[7] Sakhare S, Perumkunnil M, Bao TH, Rao S, Kim W, Crotti D, et al. Enablement of STT-MRAM as Last Level Cache for the High Performance Computing Domain at the 5nm Node. Proc. of the 2018 IEDM 2018. https://doi.org/10.1109/IEDM.2018.8614637. pp. 18.3.1–18.3.4.

[8] Garello K, Yasin F, Couet S, Souriau L, Swerts J, Rao S, et al. SOT-MRAM 300MM Integration for Low Power and Ultrafast Embedded Memories. Proc. of the 2018 IEEE Symposium on VLSI Circuits 2018. p. 81–2. https://doi.org/10.1109/VLSIC.2018.8502269.

[9] Garello K, Avci CO, Miron IM, Baumgartner M, Ghosh A, Auffret S, et al. Ultrafast magnetization switching by spin-orbit torques. Appl Phys Lett 2014;105:212402https://doi.org/10.1063/1.4902443.

[10] Łazarski S, Skowroski W, Kanak J, Karwacki L, Zietek S, Grochot K, et al. Field-Free Spin-Orbit-Torque Switching in Co/Pt/Co Multilayer with Mixed Magnetic Anisotropies. Phys. Rev. Applied 2019;12:014006https://doi.org/10.1103/PhysRevApplied.12.014006.

[11] Garello K, Yasin F, Couet S, Hody H, Souriau L, et al. Manufacturable 300mm Platform Solution for Field-Free Switching SOT-MRAM. Proc. of the 2019 Symposium on VLSI Circuits 2019. p. T194–5. https://doi.org/10.23919/VLSIC.2019.8778100.

[12] Fukami S, Zhang C, DuttaGupta S, Kurenkov A, Ohno H. Magnetization switching by spin-orbit torque in an antiferromagnet-ferromagnet bilayer system. Nature Mater 2016;15:535–41. https://doi.org/10.1038/nmat4566.

[13] van den Brink A, Vermijs G, Solignac A, Koo J, Kohlhepp JT, Swagten HJM, Koopmans B. Field-free magnetization reversal by spin-hall effect and exchange bias. Nature Commun 2016;7:10854. https://doi.org/10.1038/ncomms10854.

[14] Lau Y-C, Betto D, Rode K, Coey JMD, Stamenov P. Spin-orbit torque switching without an external field using interlayer exchange coupling. Nature Nanotechnol 2016;11:758–62. https://doi.org/10.1038/nnano.2016.84.

[15] Safeer CK, Lopez EJA, Buda-Prejbeanu L, Auffret S, Pizzini S, Boulle O, G. Gaudin IM. Spin-orbit torque magnetization switching controlled by geometry. Nature Nanotechnol 2016;11:143–6. https://doi.org/10.1038/nnano.2015.252.

[16] Oh Y-W, Baek S-HC, Kim YM, Lee HY, Lee K-D, Yang C-G, et al. Field-Free Switching of Perpendicular Magnetization through Spin-Orbit Torque in Antiferromagnet/Ferromagnet/Oxide Structures. Nature Nanotechnology 2016;11:878–84. https://doi.org/10.1038/nnano.2016.109.

[17] MacNeill D, Stiehl GM, Guimaraes MHD, Buhrman RA, Park J, Ralph DC. Control of spin-orbit torques through crystal symmetry in WTe2/ferromagnet bilayers. Nature Phys 2016;13:300–5. https://doi.org/10.1038/nphys3933.

[18] Torrejon J, Garcia-Sanchez F, Taniguchi T, Sinha J, Mitani S, Kim J-V, Hayashi M. Current-driven asymmetric magnetization switching in perpendicularly magnetized CoFeB/MgO heterostructures. Phys Rev B 2015;91:214434https://doi.org/10.1103/PhysRevB.91.214434.

[19] Yu G, Upadhyaya P, Fan Y, Alzate JG, Jiang W, Wong KL, et al. Switching of perpendicular magnetization by spin-orbit torques in the absence of external magnetic fields. Nature Nanotechnol 2014;9:548–54. https://doi.org/10.1038/nnano.2014.94.

[20] Yu G, Chang L-T, Akyol M, Upadhyaya P, He C, Li X, et al. Current-Driven Perpendicular Magnetization Switching in Ta/CoFeB/[TaOx or MgO/TaOx] Films with Lateral Structural Asymmetry. App. Phys. Lett. 2014;105:102411https://doi.org/10.1063/1.4895735.

[21] Ma Q, Li Y, Gopman DB, Kabanov YP, Shull RD, Chien CL. Switching a perpendicular ferromagnetic layer by competing spin currents. Phys Rev Lett 2018;120:117703https://doi.org/10.1103/PhysRevLett.120.117703.

[22] Sverdlov V, Makarov A, Selberherr S. Two-pulse sub-ns switching scheme for advanced spin-orbit torque MRAM. Solid-State Electron 2019;155:49–56. https://doi.org/10.1016/j.sse.2019.03.010.

[23] Sverdlov V, Makarov A, Selberherr S. Reliable sub-nanosecond switching of a perpendicular SOT-MRAM cell without external magnetic field. J Systemics, Cybern Inform 2018;16:55–9.

[24] Miron IM, Garello K, Gaudin G, Zermatten P-J, Costache MV, Auffret S, et al. Perpendicular Switching of a Single Ferromagnetic Layer Induced by In-Plane Current Injection. Nature 2011;476:189–93. https://doi.org/10.1038/

nature10309.

[25] Garello K, Miron IM, Avci CO, Freimuth F, Mokrousov Y, Blügel S, et al. Symmetry and Magnitude of Spin-Orbit Torques in Ferromagnetic Heterostructures. Nature Nanotechnology 2013;8:587–93. https://doi.org/10.1038/nnano.2013.145.

[26] Safranski C, Montoya EA, Krivorotov IN. Spin-orbit torque driven by a planar hall current. Nature Nanotechnol 2019;14:27–30. https://doi.org/10.1038/s41565-018-0282-0.

[27] Yoon J, Lee S-W, Kwon JH, Lee JM, Son J, Qiu X, et al. Anomalous spin-orbit torque switching due to field-like torque-assisted domain wall reflection. Sci Adv 2017;3:1–6. https://doi.org/10.1126/sciadv.1603099.

[28] Watanabe K, Jinnai B, Fukami S, Sato H, Ohno H. Shape anisotropy revisited in single-digit nanometer magnetic tunnel junctions. Nature Commun 2018;9:663. https://doi.org/10.1038/s41467-018-03003-7.

[29] Aharoni A. Demagnetizing factors for rectangular ferromagnetic prisms. J Appl Phys 1998;83:3432–4. https://doi.org/10.1063/1.367113.

[30] Ikegami K, Noguchi H, Takaya S, Kamata C, Amano M, Abe K, et al. MTJ-Based Normally-Off Processors with Thermal Stability Factor Engineered Perpendicular MTJ, L2 Cache Based on 2T–2MTJ Cell, L3 and Last Level Cache Based on 1T–1MTJ Cell and Novel Error Handling Scheme. Proc. of the 2015 IEDM 2015. https://doi.org/10.1109/IEDM.2015.7409762. pp. 25.1.1–25.1.4.

[31] ViennaMag, 2016. www.iue.tuwien.ac.at/index.php?id=24.

[32] Makarov A, Modeling of Emerging Resistive Switching Based Memory Cells, Ph.D. thesis, Institute for Microelectronics, TU Wien, Vienna, 2014. www.iue.tuwien.ac.at/phd/makarov/.

[33] de Orio RL, Makarov A, Goes W, Ender J, Fiorentini S, Sverdlov V, Physica B: Condensed Matter (2019). Accepted.